

Article

# Investigation on Atomic Structure and Mechanical Property of Na- and Mg-Montmorillonite under High Pressure by First-Principles Calculations

Jian Zhao <sup>1,2,3</sup>, Yu Cao <sup>1,2</sup>, Lei Wang <sup>1,2</sup>, Hai-Jiang Zhang <sup>3,4,\*</sup> and Man-Chao He <sup>1</sup>

<sup>1</sup> State Key Laboratory of Geomechanics and Deep Underground Engineering, China University of Mining and Technology, Beijing 100083, China; zhaojian@cumtb.edu.cn (J.Z.); caoyu@student.cumtb.edu.cn (Y.C.); 1810630609@student.cumtb.edu.cn (L.W.); manchaohecumtb@163.com (M.-C.H.)

<sup>2</sup> School of Mechanics and Civil Engineering, China University of Mining and Technology, Beijing 100083, China

<sup>3</sup> Key Laboratory of Rock Mechanics and Geohazards of Zhejiang Province, Shaoxing University, Shaoxing 312009, China

<sup>4</sup> Zhejiang Collaborative Innovation Center for Prevention and Control of Mountain Geologic Hazards, Shaoxing 312009, China

\* Correspondence: haijiang1086@usx.edu.cn

**Abstract:** Montmorillonite is an important layered phyllosilicate material with many useful physico-chemical and mechanical properties, which is widely used in medicine, environmental protection, construction industry, and other fields. In order to get a better understanding of the behavior of montmorillonite under high pressure, we studied its atomic structure, electronic and mechanical properties using density functional theory (DFT), including dispersion corrections, as a function of the interlayer Na and Mg cations. At ideal condition, the calculations of lattice constants, bond length, band structure, and elastic modulus of Na- and Mg-montmorillonite are in good agreement with the experimental values. Under high pressure, the lattice constants and major bond lengths decreased with increasing pressure. The calculated electronic properties and band structure show only a slight change under 20 GPa, indicating that the effect of pressure on the electronic properties of Na- and Mg-montmorillonite is weak. The bulk modulus, shear modulus, Young's modulus, shear wave velocity and compression wave velocity of Na- and Mg-montmorillonite are positively correlated with the external pressure, and the other mechanical parameters have a little change. The calculated studies will be useful to explore experiments in the future from a purely scientific point of view.

**Keywords:** first-principles calculations; mechanical property; electronic property; atomic structure; montmorillonite



**Citation:** Zhao, J.; Cao, Y.; Wang, L.; Zhang, H.-J.; He, M.-C. Investigation on Atomic Structure and Mechanical Property of Na- and Mg-Montmorillonite under High Pressure by First-Principles Calculations. *Minerals* **2021**, *11*, 613. <https://doi.org/10.3390/min11060613>

Academic Editors: Anna Pakhomova and Ilya Kuppenko

Received: 13 May 2021

Accepted: 4 June 2021

Published: 8 June 2021

**Publisher's Note:** MDPI stays neutral with regard to jurisdictional claims in published maps and institutional affiliations.



**Copyright:** © 2021 by the authors. Licensee MDPI, Basel, Switzerland. This article is an open access article distributed under the terms and conditions of the Creative Commons Attribution (CC BY) license (<https://creativecommons.org/licenses/by/4.0/>).

## 1. Introduction

Phyllosilicate minerals are an important class of layered materials that have long benefitted human life and civilization and are commonly used in many fields. With an increasing understanding of clays' physicochemical and mechanical properties, clays are realized as viable for an enhanced performance in a variety of materials and products in the areas of catalysis, food additives, antibacterial functions, polymers, sorbents, and other fields [1–5]. Montmorillonite is one of the most abundant components in clays [6]. Significant development in the use and application of montmorillonite is seen in recent times. Montmorillonite has the following characteristics: (1) colloidal-size particles, (2) high specific surface area; (3) moderate layer charge; (4) large cation exchange capacity, (5) variable interlayer separation; (6) propensity for intercalating extraneous substances [7]. Therefore, montmorillonite plays an important role in wastewater treatment, pharmaceutical industry, cosmetics, and mining operations [8–11]. On the other hand, montmorillonite

has been gradually applied in the field of nanocomposites, forming a new type of material, namely polymer/montmorillonite nanocomposites [4], as it has a non-traditional nanocomposite structure and shows better physical and mechanical properties [12,13], barrier properties [14,15], and adsorption [16]. All above applications are related to the physicochemical and mechanical properties of montmorillonite, so it is of great significance to understand the atomic structure, and electronic and elastic properties of montmorillonite for researchers in the fields of geophysics and geomechanics.

A series of experimental studies have investigated the structure and elastic modulus of montmorillonite. Hofmann et al. [17] suggested a crystal structure for montmorillonite and demonstrated that the adsorption of water made the unit cell expand along the *c* axis. Mooney et al. [18] studied the evolution of the interlayer spacing of montmorillonite by X-ray diffraction. Cowley and Goswami [19] found that the lattice constants *a* and *b* of montmorillonite samples increased by 2% after interlayer organic additives were added by convergent-beam electron diffraction. Transmission electron microscopy data investigated by Nadeau et al. [20] showed that the thickness of a single 2:1 silicate layer was only ~10 Å in the Wyoming montmorillonite samples. Wang et al. [21] designed a method of measuring elastic properties of solid clays and had successfully extracted effective elastic properties of montmorillonite from measurements made on two-component composite samples. In order to eliminate the effect of temperature and polar compounds on the structure of clay minerals, Vanorio et al. [22] studied the elastic properties of montmorillonite by acoustic measurement of cold pressed samples, and measured the bulk modulus and shear modulus of montmorillonite as 6–11 GPa and 4–6 GPa, respectively. Mondol et al. [23] calculated elastic parameters of montmorillonite based on empirical extrapolation of experimental measurements of the changes in porosity, density and acoustic velocity with the increasing vertical effective stress. These experimental results are helpful to understand the elastic properties of montmorillonite to some extent. However, due to the disordered stacking and small grain particle size of montmorillonite, it is still difficult to measure the accurate values of atomic structure and elastic parameters by experiment.

With the development of theoretical research, first-principles calculation based on density functional theory (DFT) has become a reliable tool for studying silicate minerals at the molecular level [24–26]. Chatterjee et al. [27] analyzed the crystal structure of montmorillonite by DFT and found that there were two distinguishable aluminum octahedral sites in the unit cell of montmorillonite. Sainz-Díaz et al. [28] studied the effect of cation substitution on structure and different octahedral cation distributions in pyrophyllite, illite and smectite by DFT methods. Chatterjee et al. [29] further investigated the effects of monovalent and bivalent cations on the swelling properties of clay structure by DFT plane wave pseudopotential method. However, there are few studies on the electronic and mechanical properties of montmorillonite under high pressure. Therefore, the purpose of this paper is to provide detailed results of electronic and mechanic properties of montmorillonite at different pressure.

Montmorillonite belongs to the smectite family of 2:1 clay mineral. It possesses net negative charge in octahedral sheet due to isomorphic substitution, that is, Mg<sup>2+</sup> substitute for Al<sup>3+</sup> [30]. Then, the negative layer charge is compensated by interlayer counterions like Na<sup>+</sup>, K<sup>+</sup>, Ca<sup>2+</sup>, Mg<sup>2+</sup>, etc. Montmorillonite is usually named after its interlayer counterion. In the present paper, the atomic and electronic structures, and mechanical properties of sodium montmorillonite (Na-MMT) and magnesium montmorillonite (Mg-MMT) were analyzed, which are commonly founded in clays. The chemical formulas of Na-MMT and Mg-MMT are Na<sub>0.5</sub>Mg<sub>0.5</sub>Al<sub>1.5</sub>Si<sub>4</sub>O<sub>10</sub>(OH)<sub>2</sub> and Mg<sub>0.75</sub>Al<sub>1.5</sub>Si<sub>4</sub>O<sub>10</sub>(OH)<sub>2</sub>, respectively. By comparing the atomic structures and elastic constants at different pressures, the effects of pressure on electronic and mechanical properties of Na-MMT and Mg-MMT were obtained.

## 2. Methods

The calculations of montmorillonite were carried out in the Vienna Ab-initio Simulation Package (VASP) code [31,32], which is based on the density functional theory

(DFT), using the projector augmented wave (PAW) pseudopotentials [33]. The exchange-correlation energy was calculated by Perdew, Burke and Ernzerhof (PBE) functional [34] within the generalized gradient approximation (GGA). To improve the accuracy of DFT for weak interactions, DFT-D2 [35] was applied to this paper. According to the calculated Hellmann–Feynman forces, all atomic positions were relaxed until the force per atom was below 0.01 eV/Å. The plane-wave cutoff energy was set at 600 eV. The  $1s^1$  of hydrogen,  $2s^2 2p^4$  of oxygen,  $3s^2 3p^1$  of aluminum,  $3s^2 3p^2$  of silicon,  $2p^6 3s^2$  of magnesium,  $2s^2 2p^6 3s^1$  of sodium were treated as valence electron. To sample the Brillouin zone, the Monkhorst–Pack scheme with a  $(3 \times 3 \times 3)$  k-point grid was adopted [36].

Elastic constant is an important parameter used to express the mechanical properties of solid materials. As stress and strain have three tensile and shear components, the elastic constant forms a  $6 \times 6$  matrix with 36 independent components [37]. According to the symmetry of the triclinic system of montmorillonite, the elastic constant is reduced to 21 independent components, including ( $C_{11}$ ,  $C_{12}$ ,  $C_{13}$ ,  $C_{14}$ ,  $C_{15}$ ,  $C_{16}$ ,  $C_{22}$ ,  $C_{23}$ ,  $C_{24}$ ,  $C_{25}$ ,  $C_{26}$ ,  $C_{33}$ ,  $C_{34}$ ,  $C_{35}$ ,  $C_{36}$ ,  $C_{44}$ ,  $C_{45}$ ,  $C_{46}$ ,  $C_{55}$ ,  $C_{56}$ , and  $C_{66}$ ). The elastic constants can be obtained by the generalized Hooke's law. After calculating the elastic constants, bulk modulus ( $B$ ) and shear modulus ( $G$ ) can be calculated according to Voigt–Reuss–Hill approximation [38]. In addition, the value of Young's modulus  $Y$ , Poisson's ratio  $\mu$ , acoustic compression ( $V_p$ ) wave velocity and shear ( $V_s$ ) wave velocity equal to  $9BG/(3B + G)$ ,  $(3B - 2G)/[2(3B + G)]$ ,  $\text{sqrt}[(3B + 4G)/(3\rho)]$ , and  $\text{sqrt}(G/\rho)$ , respectively.

### 3. Results and Discussion

#### 3.1. Atomic Structure and Mechanical Property of Na-MMT and Mg-MMT at Ideal Condition

Montmorillonite is a 2:1 type dioctahedral layered aluminosilicate mineral. Its layered structure consists of stacked layers, which were mainly linked by van der Waals force and electrostatic force [39]. Each layer is composed of two silicon-oxygen tetrahedral sheets sandwiching one aluminum (magnesium)-oxygen octahedral sheet. The tetrahedral sheet is linked to adjacent tetrahedrons by sharing three corners forming a hexagonal network, and the remaining corner is shared with octahedron of adjacent octahedral sheet [6]. The aluminum (magnesium)-oxygen octahedron is connected by oxygen or hydroxyl to form an octahedral sheet. In the present, the calculation models of Na-MMT and Mg-MMT taking  $\text{Na}_{0.5}\text{Mg}_{0.5}\text{Al}_{1.5}\text{Si}_4\text{O}_{10}(\text{OH})_2$  and  $\text{Mg}_{0.75}\text{Al}_{1.5}\text{Si}_4\text{O}_{10}(\text{OH})_2$  as ideal chemical formulas were constructed. The crystal structure of Na-MMT and Mg-MMT are shown in Figure 1a,b, respectively. The unit cell of Na-MMT is composed of 82 atoms (6 Al atoms, 2 Mg atoms, 2 Na atoms, 16 Si atoms, 8 H atoms and 48 O atoms). The unit cell of Mg-MMT is composed of 81 atoms (6 Al atoms, 3 Mg atoms, 16 Si atoms, 8 H atoms and 48 O atoms). The calculated structural parameters of Na-MMT ( $2a = 10.5 \text{ \AA}$ ,  $b = 9.07 \text{ \AA}$ ,  $c = 9.98 \text{ \AA}$ ,  $\alpha = 83.48^\circ$ ,  $\beta = 97.16^\circ$ ,  $\gamma = 89.88^\circ$ ) and Mg-MMT ( $2a = 10.49 \text{ \AA}$ ,  $b = 9.06 \text{ \AA}$ ,  $c = 9.69 \text{ \AA}$ ,  $\alpha = 81.12^\circ$ ,  $\beta = 96.95^\circ$ ,  $\gamma = 89.85^\circ$ ) were listed in Table 1. The calculated results are in good agreement with the existing data [40,41]. The exchange-correlation functional used in Ref. [41] was DFT-D2, which was consistent with this work. The lattice  $c$  of Na-MMT is larger than the value of Mg-MMT.

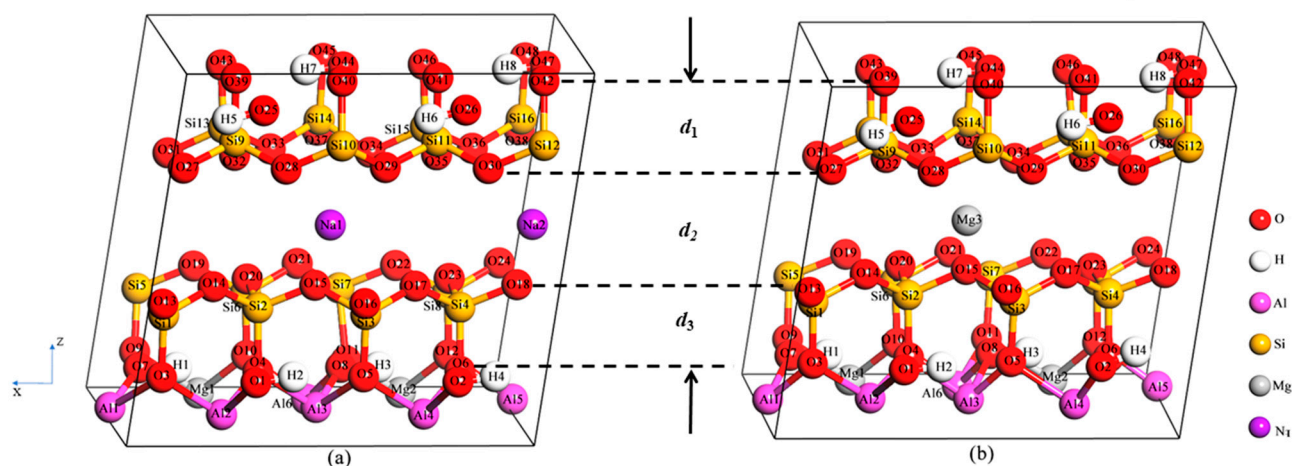


**Figure 1.** Unit cell of the Na-MMT (a) and Mg-MMT (b). White spheres = hydrogen; red spheres = oxygen; purple spheres = sodium; grey spheres = magnesium; yellow spheres = silicon and magenta spheres = aluminum.  $d_1$  and  $d_3$ —layer thickness of silicon oxide tetrahedral sheet,  $d_2$ —interlayer thickness.

**Table 1.** Calculated lattice parameters of the Na-MMT and Mg-MMT using basis sets were described in present study.

Type	Phase	2a(Å)	b(Å)	c(Å)	$\alpha$ (deg)	$\beta$ (deg)	$\gamma$ (deg)
Na-MMT	This work	10.50	9.07	9.98	83.48	97.16	89.88
	Experiment [40]	10.36	8.98	10.10	90.00	99.50	90.00
	Calculated [41]	10.45	9.07	9.57	99.37	99.18	90.14
Mg-MMT	This work	10.49	9.06	9.69	81.12	96.95	89.95
	Calculated [41]	10.39	9.02	9.30	80.60	96.47	89.75

The major bond lengths of Na-MMT and Mg-MMT in ideal condition (0 K and 0 GPa) were listed in Table 2. According to the difference of the connected atoms, the oxygen atoms are divided into five kinds:  $O_a$  is an oxygen atom connected to Al, Mg and H atom;  $O_b$  is an oxygen atom connected to one H atom and two Al atoms;  $O_c$  is an oxygen atom connected only to Si atom.  $O_d$  is an O atom connected to Al, Mg and Si atom;  $O_e$  is an O connected to two Al atoms and one Si atom. The result showed the length of O-Si bonds were shorter than that of O-Al bonds, which indicated that the strength of Al-O bonds was weaker than that of Si-O bonds. The length of  $O_d$ -Mg bonds was longer than  $O_d$ -Al and  $O_e$ -Al bonds, which implied that  $Mg^{2+}$  instead of  $Al^{3+}$  reduces the connection strength between aluminum–oxygen octahedron and silicon–oxygen tetrahedron.

**Table 2.** The bond lengths (Å) in optimized structure of the Na-MMT and Mg-MMT at ideal condition.

Bond	O-H	$O_a$ -Al	$O_a$ -Mg	$O_b$ -Al	$O_c$ -Si	$O_d$ -Si	$O_d$ -Al	$O_d$ -Mg	$O_e$ -Si	$O_e$ -Al
Na-MMT	0.972	1.858	2.057	1.925	1.639	1.613	1.936	2.082	1.645	1.966
Mg-MMT	0.971	1.857	2.049	1.919	1.643	1.611	1.912	2.081	1.645	1.963

The electrical conductivity of materials is related to the width of the forbidden band, which is the lowest energy required for electrons to transition from valence band to conduction band. The band structure of montmorillonite was analyzed to study conductivity. The band structures of Na-MMT and Mg-MMT along high-symmetry lines of the Brillouin zone (BZ) were plotted in Figure 2a,b. The high symmetry points were G (0,0,0), F (0,0.5,0), Q (0,0.5,0.5) and Z (0,0,0.5), respectively. The Fermi energy level was set at zero. The top of valence band of Na-MMT is at Q, and the bottom of the conduction band is at G. The top of the valence band of Mg-MMT is at F, and the bottom of the conduction band is at G. The result showed they all had indirect band gap. The band gap widths of Na-MMT and Mg-MMT were 4.79 eV and 4.51 eV, respectively, and the band gap width of Na-MMT

was significantly larger than Mg-MMT, as shown in Figure 2. The results indicated that the electrons of Na-MMT were more difficult to transition from the valence band to the conduction band than the electrons of Mg-MMT.

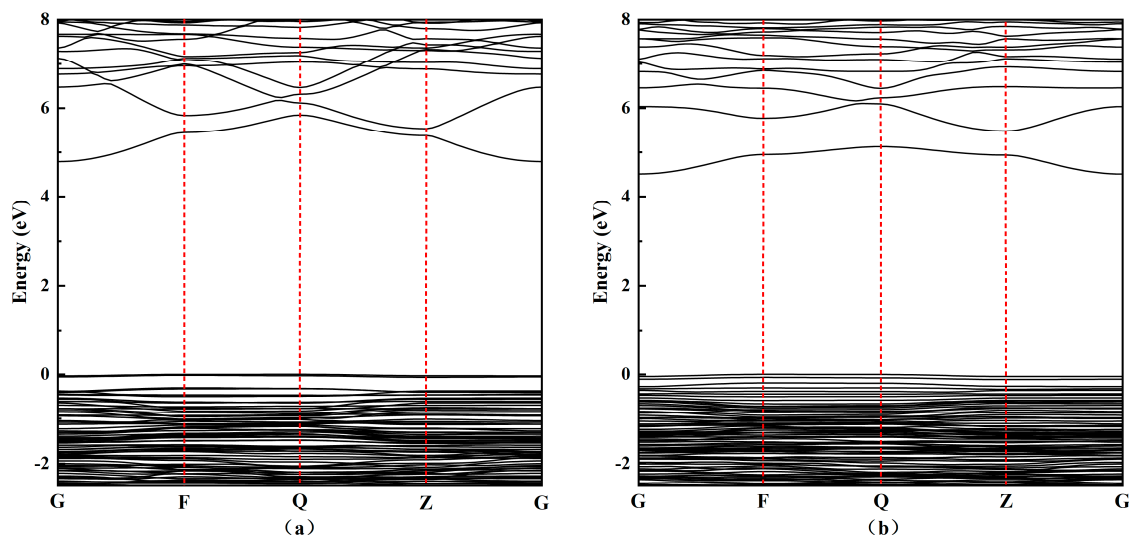


**Figure 2.** Band structure of the Na-MMT (a) and Mg-MMT (b) along high-symmetry points in the Brillouin zone at 0 GPa. The Fermi energy was set at zero.

The density of states is the number of electronic states per unit energy near a certain energy, which can reflect the occupation of electrons in each orbital and serve as a visual result of the band structure. The total density of states (TDOS) and projected density of states (PDOS) of Na-MMT and Mg-MMT were depicted in Figure 3. Five different types of oxygen atoms were drawn in a density of states diagram. The results showed that the PDOS curves of the five oxygen atoms were similar, which due to the high ionicity of oxygen atoms, leading to charge transfer from the Al 3*p*, the Si 3*p* and Mg 3*s* states to O 2*p* states. The analysis of the projected density of states (PDOS) revealed that the valence band of Na-MMT and Mg-MMT was mainly comprised of oxygen *p* states in the wide energy range of  $-10$  eV to 0 eV. In addition to the contribution of the *p* states of oxygen to the valence band, there was also a small part of the contribution of the *s* and *p* states of Al, Si and Mg. By comparing the density of states of Na-MMT and Mg-MMT, it can be found that the type of interlayer cations has little effect on the density of states.

To understand further the charge distribution among the different atoms in Na-MMT and Mg-MMT, the orbital distribution of montmorillonite at high-symmetry BZ points G, F, Q and Z were studied, as shown in Tables 3 and 4, respectively. The results showed that the VBMs of Na-MMT at each high symmetry point was mainly composed of the 2*p* states of O. The CBMs at the F and Q (denoted by F(c) and Q(c) in Table 3) was mainly composed of the 2*s*, 2*p* states of O and the 3*s* states of Al, Si, Na and Mg, while the G(c) and Z(c) were mainly composed of the 2*p* states of O. It was found from Table 4 that the VBMs and CBMs of each high symmetry point in Mg-MMT were mainly composed of the 2*p* states of O. The sum of all the PDOS value for O and H for each high-symmetry points of Na-MMT is 4.38 eV and 0.05 eV by calculation, respectively. The electronic states from O represent 14% of the total electronic states at G(v), 16% of the states at G(c), 14% of the states at F(v), 5% of the states at F(c), 14% of the states at Q(v), 6% of the states at Q(c), 14% of the states at Z(v), and 16% of the states at Z(c). The sum of all the PDOS value for O and H for each high-symmetry points of Mg-MMT is 5.198 eV and 0.038 eV by calculation, respectively. The electronic states from O represent 11% of the total electronic states at G(v), 13% of the states at G(c), 11% of the states at F(v), 14% of the states at F(c), 12% of the states at Q(v), 14% of the states at Q(c), 12% of the states at Z(v), and 14% of the states at Z(c).

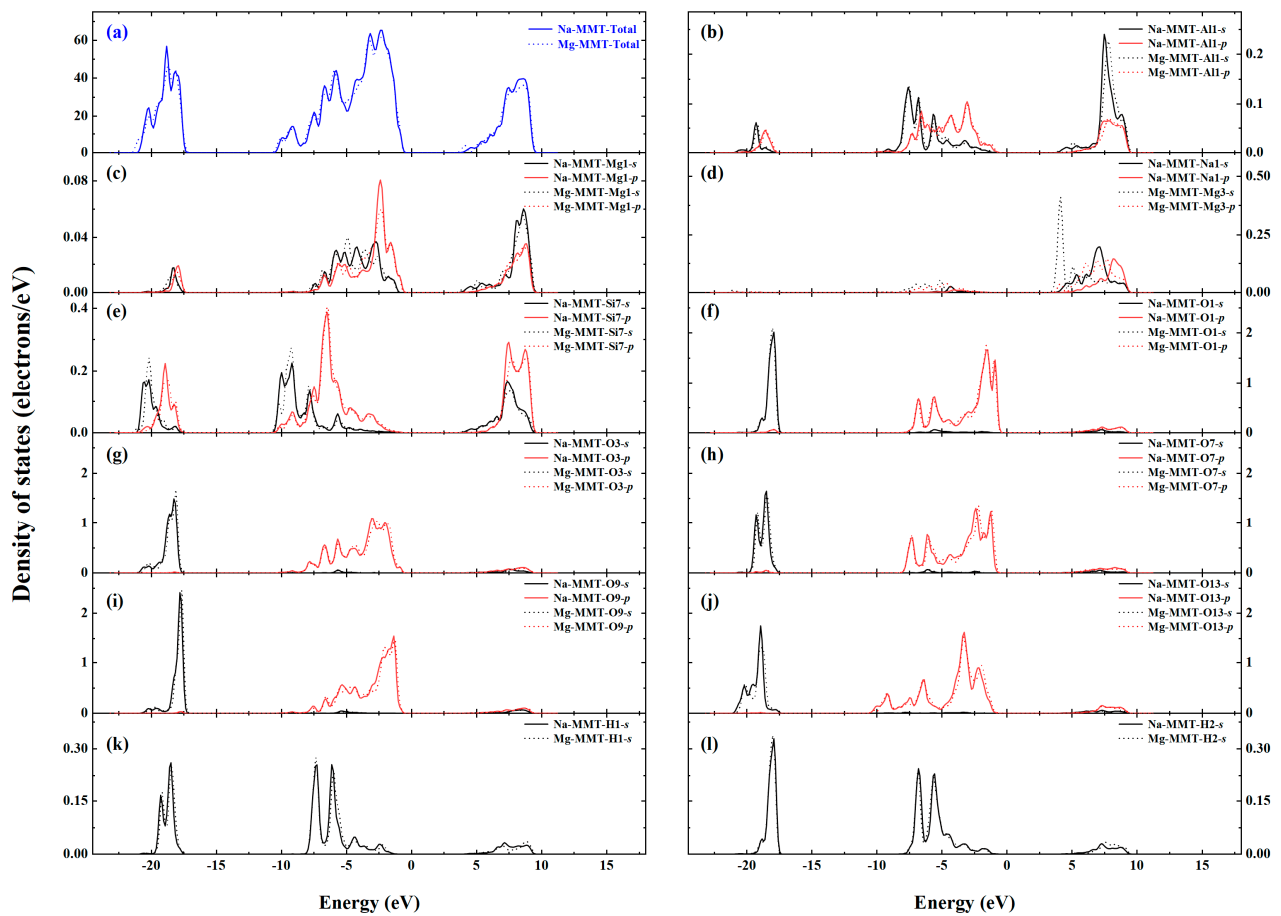


Figure 3. The total density of states (a) and partial density of states (b–l) of the Na-MMT and Mg-MMT at 0 GPa.

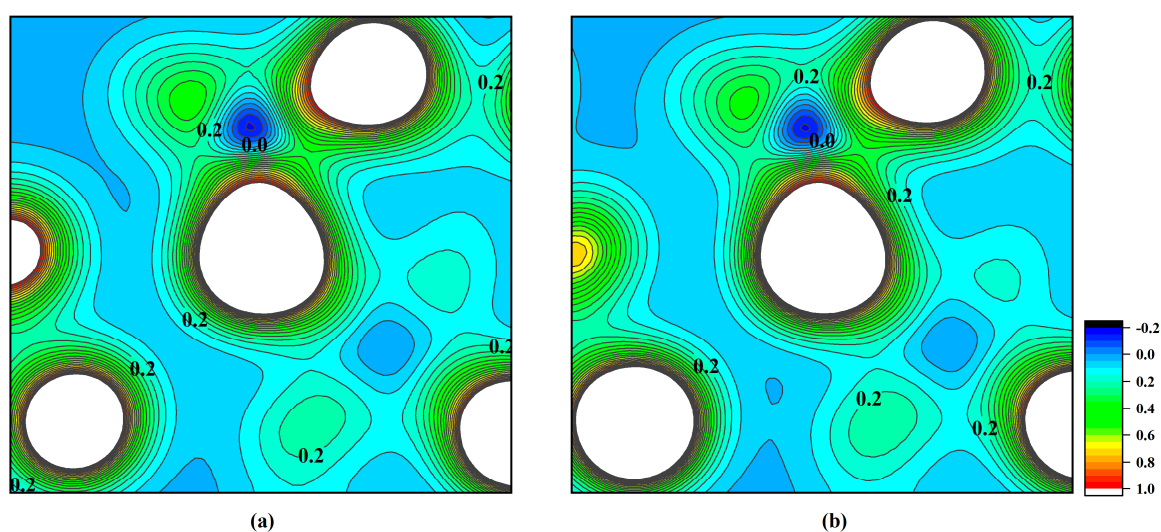
Table 3. Calculated orbital-decomposed site (atom)-projected electron charges inside the muffin-tin spheres of the Na-MMT at the high-symmetry (HS) BZ points G, F, Q, and Z.

HS Point	Site	s	p	HS Point	Site	s	p	HS Point	Site	s	p	HS Point	Site	s	p
G(v)	Al1	0	0.003	G(c)	Al1	0	0	F(v)	Al1	0.001	0.003	F(c)	Al1	0.005	0
	Mg1	0	0		Mg1	0	0.001		Na1	0	0		Na1	0.021	0
	O1	0	0.002		O1	0	0.136		Si1	0	0.003		Si1	0.003	0
	O3	0	0.016		O3	0	0.008		O1	0	0.001		O1	0	0.004
	O7	0	0.032		O7	0	0		O3	0	0.009		O3	0.003	0.001
	O9	0.001	0.008		O9	0	0.009		O7	0	0.010		O7	0.006	0.001
	O13	0	0.010		O13	0	0.003		O9	0	0.007		O9	0.001	0.002
	H1	0	0.001		H1	0	0		O13	0	0.009		O13	0	0.003
H2	0	0	H2	0	0.002	H1	0.002	0	H1	0.001	0.002				
Q(v)	Al1	0	0.001	Q(c)	Al1	0.005	0	Z(v)	Al1	0	0.001	Z(c)	Al1	0	0
	Mg1	0	0		Mg1	0.002	0		Mg1	0.001	0		Mg1	0	0.001
	Na1	0	0		Na1	0.009	0.001		Na1	0	0		Na1	0	0
	Si1	0	0.001		Si1	0.007	0		Si1	0	0.001		Si1	0	0
	O1	0	0.001		O1	0.005	0.003		O1	0	0.002		O1	0	0.136
	O3	0.001	0.009		O3	0.006	0.001		O3	0	0.002		O3	0	0.009
	O7	0	0.006		O7	0.007	0.003		O7	0	0.012		O7	0	0
	O9	0	0.013		O9	0.004	0.002		O9	0	0.007		O9	0	0.009
O13	0.001	0.063	O13	0.006	0.003	O13	0	0.010	O13	0	0.003				
H1	0	0	H1	0.001	0.002	H1	0	0	H2	0	0				
H2	0	0	H2	0.001	0.002	H2	0	0	H2	0	0.002				

**Table 4.** Calculated orbital-decomposed site (atom)-projected electron charges inside the muffin-tin spheres of the Mg-MMT at the high-symmetry (HS) BZ points G, F, Q, and Z.

HS Point	Site	<i>s</i>	<i>p</i>	HS Point	Site	<i>s</i>	<i>p</i>	HS Point	Site	<i>s</i>	<i>p</i>	HS Point	Site	<i>s</i>	<i>p</i>
G(v)	Al1	0	0.001	G(c)	Al1	0	0	F(v)	Al1	0	0.001	F(c)	Al1	0	0.001
	Mg3	0	0		Mg3	0	0		Si1	0	0.002		Si1	0	0
	O1	0.001	0.002		O1	0	0.013		O1	0	0.002		O1	0	0.010
	O3	0	0.002		O3	0	0.001		O3	0	0.021		O3	0	0.002
	O7	0	0.001		O7	0	0		O7	0.001	0.007		O7	0	0.001
	O9	0	0.001		O9	0	0.003		O9	0	0.021		O9	0	0.002
O13	0	0.014	O13	0	0.002	O13	0.001	0.048	O13	0	0.001				
Q(v)	Al1	0	0.001	Q(c)	Al1	0	0.001	Z(v)	Al1	0	0.002	Z(c)	Al1	0	0
	Mg3	0	0		Mg3	0	0		Mg3	0	0.001		Mg3	0	0
	O1	0	0.001		O1	0	0.016		O1	0	0.005		O1	0	0.026
	O3	0	0.003		O3	0	0.003		O3	0	0.006		O3	0	0.002
	O7	0	0.001		O7	0	0.002		O7	0	0.002		O7	0	0
	O9	0	0.006		O9	0	0.003		O9	0	0.001		O9	0	0.003
	O13	0	0.007		O13	0	0.002		O13	0	0.009		O13	0	0.002
H1	0	0	H1	0	0	H1	0.001	0	H1	0	0				

To understand the bonding properties and charge distribution of atoms in Na-MMT and Mg-MMT system more intuitively, the charge density diagrams of Na-MMT and Mg-MMT were drawn in Figure 4a,b, respectively. Figure 4 showed a charge density diagram of the montmorillonite crystal located at the Al6-O11-Si7 plane, and O11 was in the center of diagram. The results showed that the charge density around the O atom was large, which indicated that the oxygen atom had high electronegativity. The oxygen atom coincided with silicon atom and Al atom in part of the charge density, indicating that the Si-O bond and Al-O bond had weak covalent bond properties. The coincidence degree of charge density between Si-O bond was higher than that of Al-O bonds, indicating that the covalent bond property of Si-O bond was stronger than that of Al-O bond. The low charge density around Al atom indicated that there was a large amount of charge transfer between Al and O, which implied that the Al-O bond was mainly characterized by an ion bond. We further analyzed Bader charges of various atoms of Na-MMT and Mg-MMT, as shown in Table 5. Mg atoms of interlayer and of octahedron were defined as Mg<sub>O</sub> and Mg<sub>I</sub>, respectively. Negative values meant the gained electrons and positive values meant the loss of electrons. It was clear that much charge transformed from Al, Si, Mg atoms to O atoms. Si atoms lost the most charge, indicating that Si-O had the strongest bonding effect.

**Figure 4.** The density of states of the Na-MMT (a) and Mg-MMT (b) at 0 GPa.

**Table 5.** Bader charges of various atoms of Na-MMT and Mg-MMT.

Type	O <sub>a</sub>	O <sub>b</sub>	O <sub>c</sub>	O <sub>d</sub>	O <sub>e</sub>	H	Al	Si	Na	Mg <sub>I</sub>	Mg <sub>O</sub>
Na-MMT	−1.43	−1.44	−1.59	−1.59	−1.60	0.61	2.48	3.15	0.87	/	1.67
Mg-MMT	−1.42	−1.43	−1.59	−1.59	−1.61	0.60	2.49	3.15	/	0.72	1.67

The elastic constant  $C_{ij}$  is essential to characterize the elasticity of the material. Some basic mechanical properties of the material can be obtained, such as bulk modulus, Young's modulus, Poisson's ratio and shear modulus through elastic constants. Na-MMT and Mg-MMT belonged to triclinic system, which had 21 independent elastic stiffness constants. The derivation results at zero temperature and zero pressure were listed in Table 6.

**Table 6.** The calculated elastic constants  $C_{ij}$  of the Na-MMT and Mg-MMT at 0 GPa.

Phase	Elastic Constants (GPa)						
Na-MMT	$C_{11}$	$C_{22}$	$C_{33}$	$C_{44}$	$C_{55}$	$C_{66}$	$C_{12}$
	173.02	210.11	27.99	7.02	10.07	56.26	50.22
	$C_{13}$	$C_{14}$	$C_{15}$	$C_{16}$	$C_{23}$	$C_{24}$	$C_{25}$
	12.54	2.07	−27.60	2.08	9.22	4.34	−8.90
Mg-MMT	$C_{26}$	$C_{34}$	$C_{35}$	$C_{36}$	$C_{45}$	$C_{46}$	$C_{56}$
	0.43	5.91	6.47	3.69	2.05	−8.92	1.42
	$C_{11}$	$C_{22}$	$C_{33}$	$C_{44}$	$C_{55}$	$C_{66}$	$C_{12}$
	170.69	198.32	69.89	17.25	18.57	57.51	60.94
Mg-MMT	$C_{13}$	$C_{14}$	$C_{15}$	$C_{16}$	$C_{23}$	$C_{24}$	$C_{25}$
	12.94	7.43	−20.84	3.18	21.63	13.84	−1.59
	$C_{26}$	$C_{34}$	$C_{35}$	$C_{36}$	$C_{45}$	$C_{46}$	$C_{56}$
5.36	9.01	13.55	−1.04	6.64	−8.25	3.37	

The elastic constants of Na-MMT were  $C_{11} = 173.02$  GPa,  $C_{22} = 210.11$  GPa and  $C_{33} = 27.99$  GPa. The elastic constant  $C_{11}$  was less than  $C_{22}$ , which indicated the anti-deformation ability of  $a$ -axis was weaker than that of  $b$ -axis. The value of  $C_{33}$  was smaller than  $C_{22}$  and  $C_{11}$ , indicating that the crystal was most likely to deform along the  $c$ -axis. Meanwhile, the elastic constants  $C_{44}$  and  $C_{55}$  were both less than  $C_{66}$  in Na-MMT, which meant the shear deformation resistance of (001) plane was stronger than that of (100) and (010) planes. As shown in Table 6, the elastic constants of Mg-MMT have the same regular to Na-MMT. These result indicated that the montmorillonite crystal was most prone to deformation along the  $c$ -axis, the anti-deformation ability of the  $a$ -axis was weaker than that of the  $b$ -axis, and the shear deformation resistance of (001) plane was stronger than that of the (100) and (010) planes. The results confirmed that the van der Waals force and electrostatic force in the interlayer were much less than the binding force between the atoms in the layer. Comparing the elastic constants of Na-MMT and Mg-MMT, the conclusions were as follows: (1) the anti-deformation ability of  $b$ -axis of Na-MMT was stronger than that of Mg-MMT, (2) the compression resistance of Na-MMT was much lower than that of Mg-MMT along  $c$ -axis, (3) the shear deformation resistance of Na-MMT was smaller than that of Mg-MMT in (100) and (010) planes.

According to the elastic constants, the mechanical parameters were calculated, as listed in Table 7, which are consistent with the experiment values [21]. The value of  $B$ ,  $Y$  and  $G$  of Na-MMT were 39.85 GPa, 55.27 GPa and 21.78 GPa, respectively, while the  $B$ ,  $Y$  and  $G$  of Mg-MMT were 58.14 GPa, 77.09 GPa and 30.71 GPa, respectively. By comparison, the results showed that the compression resistance, shear resistance and stiffness of Mg-MMT were greater than those of Na-MMT. Pugh's modulus ( $G/B$ ) is used to represent the ductile–brittle property of material. When  $G/B < 0.57$ , the material shows good ductility [42]. The  $G/B$  values of Na-MMT and Mg-MMT were 0.547 and 0.518, respectively, indicating that montmorillonite had good ductility. Vicker's hardness is a standard of material hardness, which can be estimated by empirical formula of  $H_v = 2(k^2G)^{0.583} - 3$ , where  $k$  is the value of

$G/B$ . The values of  $H_V$  were 2.96 GPa and 3.76 GPa for Na-MMT and Mg-MMT, respectively, which indicated the hardness of Mg-MMT was larger than that of Na-MMT. The calculated values of  $\mu$  were 0.269 and 0.275 for Na-MMT and Mg-MMT, respectively. The acoustic compression wave velocity ( $V_p$ ) and shear wave velocity ( $V_s$ ) were also calculated, which were critical for analysis of seismic exploration data and interpretation of acoustic scattering measurements [43]. These above calculated data were in good agreement with the previous experimental data [21].

**Table 7.** The calculated bulk modulus ( $B$ ), shear modulus ( $G$ ), Young's modulus ( $Y$ ), Poisson's ratio ( $\mu$ ), Pugh's modulus ( $G/B$ ), Vicker's hardness ( $H_V$ ), compression wave velocity ( $V_p$ ), and shear wave velocity ( $V_s$ ) of the Na-MMT and Mg-MMT compared with experimental data. / means that the relevant value is not given in Reference [21].

Mechanical Quantity	Na-MMT	Mg-MMT	Experiment [21]	
			Na-MMT	Mg-MMT
Bulk modulus $B$ (GPa)	39.85	58.14	34.7	63.4
Young's modulus $Y$ (GPa)	55.27	77.09	/	/
Shear modulus $G$ (GPa)	21.78	30.13	20.3	26.2
Poisson's ratio $\mu$	0.269	0.279	0.255	0.318
Compression wave velocity $V_p$ (km/s)	5.12	6.06	4.88	6.07
Shear wave velocity $V_s$ (km/s)	2.88	3.35	2.80	3.13
Pugh's modulus $G/B$ ratio	0.547	0.518	/	/
Vickers hardness $H_V$ (GPa)	2.96	3.76	/	/

### 3.2. Effects of Pressure on Atomic Structure and Mechanical Properties of Na-MMT and Mg-MMT

To avoid Pulay stress problems, the geometric optimization of each pressure state is performed at a fixed volume rather than at a constant pressure. In the present paper, the total energy ( $E$ ) of Na-MMT at a serial of volumes as  $V_0$  ( $V_0$  is the equilibrium volume at ideal condition),  $0.99V_0$ ,  $0.98V_0$ ,  $0.97V_0$ ,  $0.96V_0$ ,  $0.95V_0$ ,  $0.94V_0$ ,  $0.93V_0$ ,  $0.925V_0$ ,  $0.92V_0$ . The total energy ( $E$ ) of Mg-MMT at a serial of volumes as  $V_0$ ,  $0.99V_0$ ,  $0.98V_0$ ,  $0.97V_0$ ,  $0.96V_0$ ,  $0.95V_0$ ,  $0.94V_0$ ,  $0.935V_0$ ,  $0.93V_0$ ,  $0.925V_0$ . Then, the  $P$ - $V$  relation was deduced by the formula  $P = -\Delta E/\Delta V$ .

The bond lengths of Na-MMT and Mg-MMT under pressure were listed in Tables 8 and 9, respectively. It can be seen that the overall trend of Si-O, Al-O, Mg-O bond length decreased with the increase of pressure, while the H-O bond length increased slightly with the increase of pressure, which was due to the influence of adjacent O atoms on hydroxyl groups under pressure. The O<sub>d</sub>-Al bond length of Na-MMT fluctuated from 15.81 GPa to 19.92 GPa. The Al-O and Mg-O bond length of Mg-MMT has a sudden change under 8.60 GPa. Furthermore, the layer distance of Na-MMT and Mg-MMT under pressure was shown in Table 10. We defined  $d_1$  and  $d_3$  as layer thickness of silicon oxygen octahedron sheet, as shown in Figure 1. The  $d_2$  represent the interlayer thickness and  $d_4$  represent aluminum (magnesium) oxide octahedral sheet. It can be seen that the interlayer thickness of Na-MMT and Mg-MMT decreased rapidly with the increase of pressure. The values of  $d_1$ ,  $d_3$  and  $d_4$  showed an overall downward trend under pressure, but the change was not obvious. The results indicated that the shrinkage of the volume of montmorillonite under pressure was mainly caused by the compression of the interlayer spacing.

**Table 8.** The bond lengths (Å) in optimized structure of the Na-MMT under pressure.

Volume	Pressure (GPa)	O-H	O <sub>a</sub> -Al	O <sub>a</sub> -Mg	O <sub>b</sub> -Al	O <sub>c</sub> -Si	O <sub>d</sub> -Si	O <sub>d</sub> -Al	O <sub>d</sub> -Mg	O <sub>e</sub> -Si	O <sub>e</sub> -Al
V <sub>0</sub>	0	0.972	1.858	2.057	1.925	1.639	1.613	1.936	2.082	1.645	1.966
0.99V <sub>0</sub>	0.87	0.972	1.857	2.054	1.927	1.637	1.612	1.907	2.075	1.644	1.961
0.98V <sub>0</sub>	2.22	0.973	1.854	2.050	1.927	1.635	1.610	1.902	2.068	1.642	1.955
0.97V <sub>0</sub>	3.96	0.973	1.850	2.042	1.926	1.632	1.608	1.894	2.059	1.639	1.949
0.96V <sub>0</sub>	6.17	0.973	1.846	2.032	1.924	1.629	1.605	1.887	2.048	1.635	1.940
0.95V <sub>0</sub>	8.90	0.974	1.841	2.023	1.919	1.625	1.602	1.879	2.035	1.631	1.931
0.94V <sub>0</sub>	12.12	0.975	1.836	2.013	1.911	1.621	1.598	1.872	2.022	1.627	1.922
0.93V <sub>0</sub>	15.81	0.979	1.837	2.006	1.894	1.614	1.600	1.875	2.015	1.662	1.916
0.925V <sub>0</sub>	17.74	0.979	1.832	2.001	1.891	1.613	1.598	1.867	2.007	1.622	1.912
0.92V <sub>0</sub>	19.92	0.980	1.829	1.994	1.886	1.611	1.597	1.879	1.985	1.620	1.906

**Table 9.** The bond lengths (Å) in optimized structure of the Mg-MMT under pressure.

Volume	Pressure (GPa)	O-H	O <sub>a</sub> -Al	O <sub>a</sub> -Mg	O <sub>b</sub> -Al	O <sub>c</sub> -Si	O <sub>d</sub> -Si	O <sub>d</sub> -Al	O <sub>d</sub> -Mg	O <sub>e</sub> -Si	O <sub>e</sub> -Al
V <sub>0</sub>	0	0.971	1.857	2.049	1.919	1.643	1.611	1.912	2.081	1.645	1.963
0.99V <sub>0</sub>	1.94	0.972	1.853	2.036	1.911	1.639	1.609	1.906	2.067	1.643	1.954
0.98V <sub>0</sub>	3.93	0.972	1.848	2.024	1.904	1.635	1.608	1.900	2.054	1.642	1.946
0.97V <sub>0</sub>	6.13	0.972	1.843	2.011	1.896	1.632	1.606	1.913	2.023	1.640	1.938
0.96V <sub>0</sub>	8.60	0.973	1.846	2.033	1.924	1.629	1.605	1.910	2.020	1.635	1.940
0.95V <sub>0</sub>	11.06	0.973	1.829	1.988	1.892	1.626	1.605	1.878	2.019	1.636	1.920
0.94V <sub>0</sub>	14.4	0.973	1.823	1.976	1.885	1.623	1.603	1.871	2.006	1.633	1.910
0.935V <sub>0</sub>	16.21	0.973	1.821	1.973	1.882	1.620	1.603	1.871	1.997	1.633	1.906
0.93V <sub>0</sub>	18.2	0.973	1.818	1.967	1.878	1.619	1.602	1.866	1.993	1.631	1.901
0.925V <sub>0</sub>	20.34	0.974	1.815	1.962	1.874	1.617	1.600	1.862	1.987	1.629	1.896

**Table 10.** The average layer thickness and interlayer thickness (Å) of Na-MMT and Mg-MMT under pressure.

		Pressure (GPa)	0	0.87	2.22	3.96	6.17	8.90	12.12	15.81	17.74	19.92
Na-MMT	<i>d</i> <sub>1</sub>		2.254	2.271	2.270	2.245	2.226	2.209	2.192	2.229	2.206	2.200
	<i>d</i> <sub>2</sub>		3.265	3.080	2.881	2.709	2.568	2.455	2.361	2.298	2.270	2.242
	<i>d</i> <sub>3</sub>		2.271	2.294	2.257	2.242	2.234	2.227	2.222	2.200	2.203	2.195
	<i>d</i> <sub>4</sub>		2.191	2.208	2.200	2.178	2.160	2.143	2.124	2.098	2.090	2.081
Mg-MMT	<i>d</i> <sub>1</sub>		2.275	2.274	2.272	2.268	2.267	2.256	2.247	2.249	2.243	2.237
	<i>d</i> <sub>2</sub>		2.951	2.852	2.758	2.670	2.586	2.508	2.432	2.394	2.359	2.328
	<i>d</i> <sub>3</sub>		2.270	2.275	2.274	2.272	2.269	2.255	2.249	2.242	2.238	2.233
	<i>d</i> <sub>4</sub>		2.199	2.197	2.196	2.195	2.185	2.191	2.185	2.180	2.176	2.172

To explore the effect of pressure on the band structure and charge density of montmorillonite, the band structure diagram and charge density diagram of Na-MMT at 19.2 GPa and Mg-MMT at 20.34 GPa were drawn, as shown in Figures 5 and 6. The valence band top and conduction band bottom of Na-MMT were still at Q point and G point, and the band gap width was 5.65 eV. The valence band top and conduction band bottom of Mg-MMT were still at F point and G point, and the band gap width was 5.29 eV. These results showed that the montmorillonite still had an indirect band gap under the pressure of about 20 GPa. The band gap width was broadened gradually, which made it more difficult for the electron to transition from the valence band to the conduction band. The same Al6-O11-Si7 plane was also selected as the charge density diagram of montmorillonite under zero pressure. As shown in Figure 6, the bonding characteristics between Si-O and Mg-O at about 20 GPa

were the same as those at 0 GPa, and the charge density between Si-O and Al-O had changed a little compared with that under 0 GPa. The total density of states (TDOS) and partial densities of states (PDOS) of Na-MMT at 19.92 GPa were drawn to explore the effect of pressure, as shown in Figure 7. The results showed the height of *sp* orbitals decreased with increasing the pressure. The results also indicated the *sp* orbitals of atoms shifted slightly down in the range below 0 eV and the *sp* orbitals of atoms shift up slightly in the energy range of 5 eV to 10 eV under the action of pressure. These above calculated results implied that the effect of pressure on density of states of montmorillonite was weak in the range of  $0 < P < 20$  GPa.

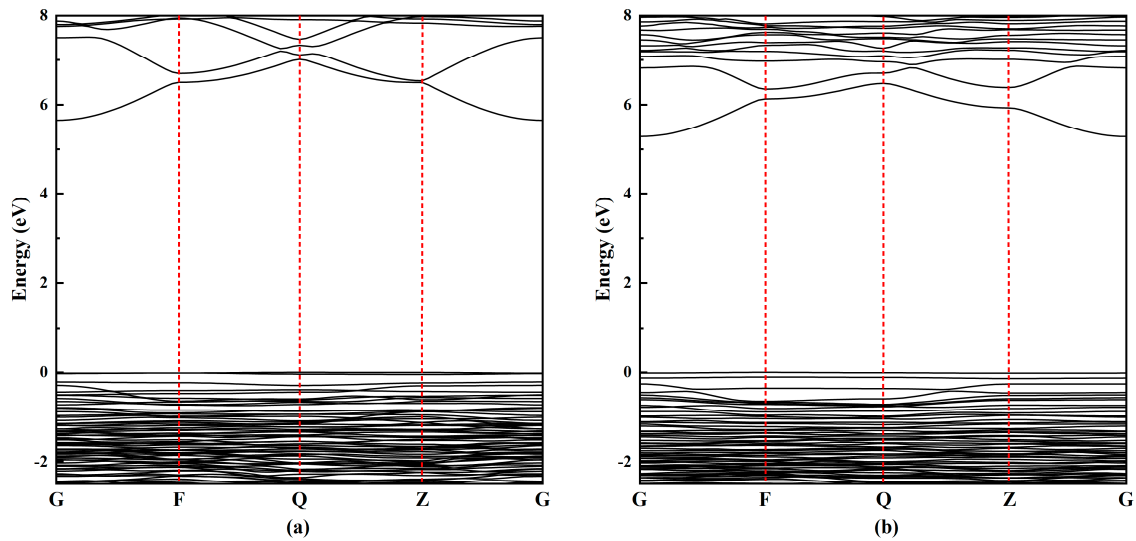


**Figure 5.** Band structure of the Na-MMT at 19.92 GPa (a) and Mg-MMT at 20.32 GPa (b) along high-symmetry points in the Brillouin zone under pressure. The Fermi energy was set at zero.

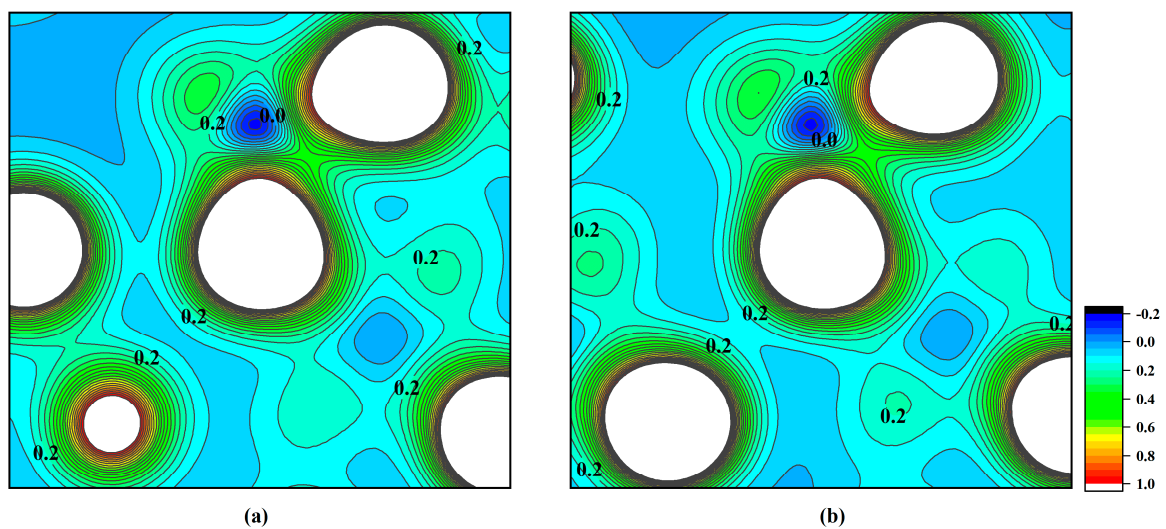


**Figure 6.** The density of states of the Na-MMT at 19.92 GPa (a) and Mg-MMT at 20.32 GPa (b).

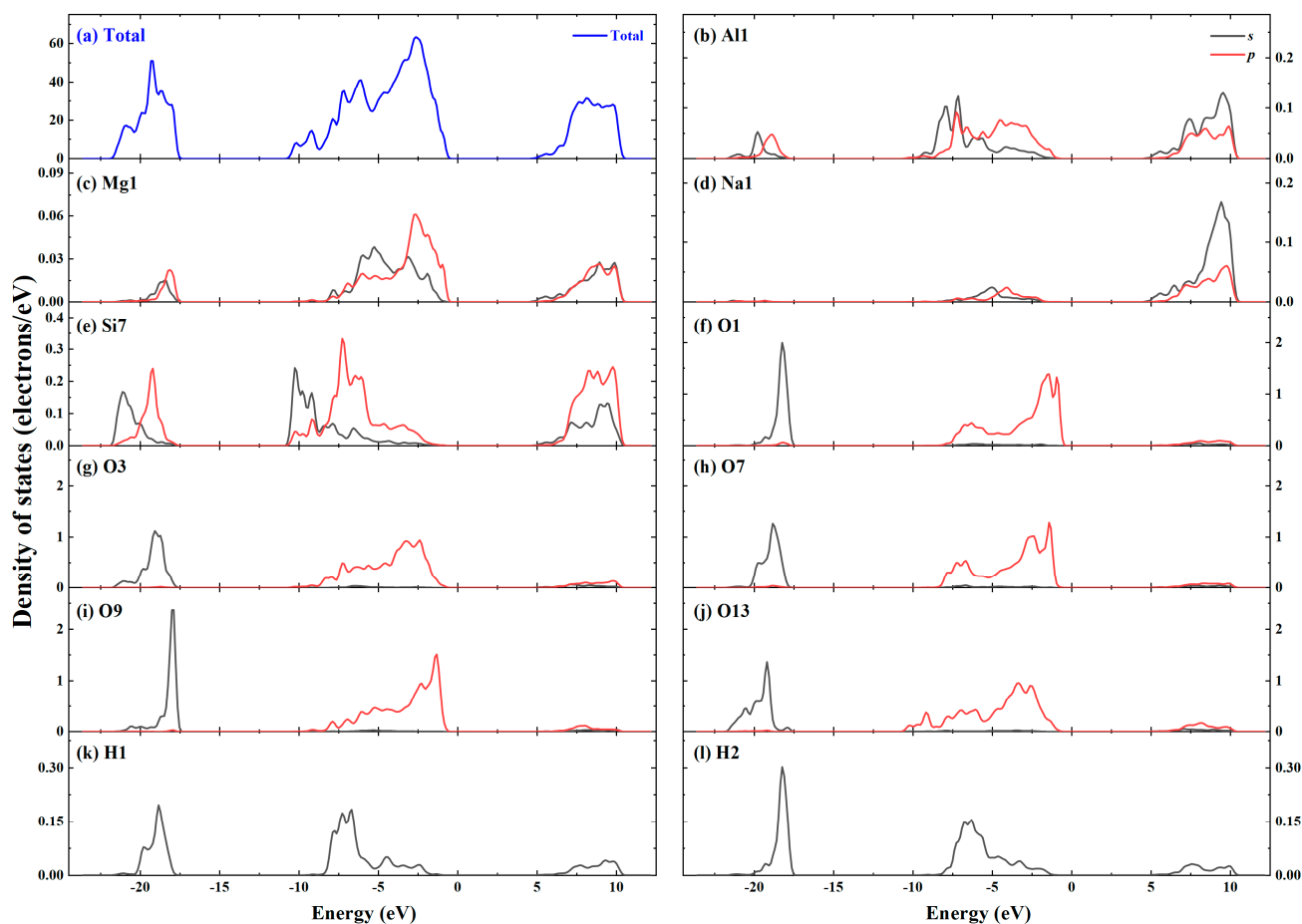


Figure 7. The total (a) and partial density (b–l) of states of Na-MMT at 19.92 GPa.

The above microscopic results of mechanical property of montmorillonite under high pressure are of great significance in the related applications fields. The elastic constants of Na-MMT and Mg-MMT under given pressure were listed in Tables 11 and 12, respectively. In order to see the change rule of elastic constant of montmorillonite in the process of pressurization more intuitively, we also drew Figure 8. The value of  $C_{11}$  and  $C_{33}$  of Na-MMT gradually increased with the increase of pressure, while  $C_{22}$  had little change, as shown in Figure 8a. When the pressure reached 15.81 GPa, the value of  $C_{33}$  was greater than that of  $C_{22}$ , which indicated that the Na-MMT crystal was easier to deform along the b-axis under the action of external force. As shown in Figure 8b, the  $C_{55}$  and  $C_{66}$  of Na-MMT increased rapidly compared with  $C_{44}$  under pressure, which indicated that the shear resistance of (010) and (001) planes of Na-MMT increased rapidly under pressure. The results showed that the overall trend of  $C_{11}$  and  $C_{22}$  of Mg-MMT increased with increasing the pressure, and  $C_{33}$  increased rapidly with the increase of pressure in Figure 8c. Figure 8d showed that  $C_{44}$  increases slowly with increasing the pressure. When the applied external pressure increased to about 16.8 GPa, the value of  $C_{55}$  was greater than that of  $C_{44}$ , indicating that the shear resistance of (010) surface is stronger than that of (100) surface.

**Table 11.** The calculated elastic constants  $C_{ij}$  of the Na-MMT under pressure.

Pressure (GPa)	0	0.87	2.22	3.96	6.17	8.90	12.12	15.81	17.74	19.92
$C_{11}$	173.02	179.18	185.87	192.64	204.10	216.54	231.56	248.99	259.90	267.22
$C_{22}$	210.11	209.16	207.51	203.62	201.00	205.95	200.47	199.60	204.98	210.60
$C_{33}$	27.99	45.97	64.64	86.92	112.84	139.88	167.80	200.98	215.27	228.96
$C_{44}$	7.02	13.24	16.10	19.52	26.15	34.02	42.25	53.28	58.15	62.42
$C_{55}$	10.07	10.54	14.14	19.43	27.12	35.84	45.82	58.30	65.19	71.09
$C_{66}$	56.26	57.93	59.81	60.53	62.67	63.70	68.02	66.93	69.35	69.61
$C_{12}$	50.22	54.31	55.76	55.93	56.12	56.16	61.18	70.45	72.72	80.48
$C_{13}$	12.54	16.59	23.28	28.52	34.20	42.64	52.51	71.59	73.74	81.18
$C_{14}$	2.07	−0.63	−2.23	−1.28	−1.78	−2.60	−4.92	−12.39	−15.08	−15.56
$C_{15}$	−27.60	−24.54	−21.88	−18.72	−15.93	−12.65	−11.21	−12.37	−9.74	−8.64
$C_{16}$	2.08	1.76	2.18	4.36	5.76	5.98	2.48	−1.99	−2.41	−2.87
$C_{23}$	9.22	15.49	18.54	29.14	38.91	43.29	51.53	55.62	62.87	67.07
$C_{24}$	4.34	4.64	2.19	3.24	2.64	−0.05	0.04	−1.80	−2.59	−3.11
$C_{25}$	−8.90	−2.81	−1.40	−1.63	−2.12	−4.33	−4.53	−1.53	1.56	−2.73
$C_{26}$	0.43	1.44	0.43	0.49	−1.01	−3.55	0.59	−7.63	−7.32	−8.04
$C_{34}$	5.91	14.60	19.27	27.92	36.20	40.54	43.62	40.43	39.91	39.22
$C_{35}$	6.47	8.41	17.37	21.82	25.12	28.80	33.15	28.12	35.21	35.52
$C_{36}$	3.69	1.18	3.03	3.59	3.45	3.95	3.46	4.14	4.27	5.03
$C_{45}$	2.05	1.81	3.07	7.10	8.40	8.64	7.86	7.19	8.25	7.26
$C_{46}$	−8.92	−8.79	−7.17	−5.71	−5.24	−4.37	−3.81	−3.54	−5.55	−4.37
$C_{56}$	1.42	2.58	2.75	4.35	4.44	4.74	2.93	2.80	1.70	2.14

**Table 12.** The calculated elastic constants  $C_{ij}$  of the Mg-MMT under pressure.

Pressure (GPa)	0	1.94	3.93	6.13	8.60	11.06	14.40	16.21	18.20	20.34
$C_{11}$	170.69	171.48	171.79	175.07	180.54	202.33	214.74	221.30	228.61	237.52
$C_{22}$	198.32	200.98	195.97	193.88	189.16	207.32	215.82	221.09	227.49	235.91
$C_{33}$	69.89	72.03	78.69	100.14	109.24	132.49	157.94	172.42	186.33	200.47
$C_{44}$	17.25	20.06	21.58	22.71	26.67	31.95	36.38	38.00	40.42	43.66
$C_{55}$	18.57	22.06	26.94	30.02	34.95	44.54	54.59	60.23	65.97	71.67
$C_{66}$	57.51	58.48	58.88	58.95	57.37	60.31	60.99	61.47	62.38	63.30
$C_{12}$	60.94	55.23	52.50	43.36	50.77	54.63	66.62	75.19	83.79	91.51
$C_{13}$	12.94	16.28	18.61	16.17	16.60	49.85	54.26	59.81	66.12	71.85
$C_{14}$	7.43	3.25	−4.18	−3.21	−3.04	−4.71	−6.50	−7.88	−9.88	−12.88
$C_{15}$	−20.84	−19.07	−18.30	−12.31	−8.20	−6.71	−5.47	−3.02	−3.45	−4.39
$C_{16}$	3.18	2.19	1.90	1.6	2.84	1.16	0.80	1.25	1.19	1.38
$C_{23}$	21.63	27.38	34.68	40.54	51.84	55.71	66.71	73.00	80.66	88.05
$C_{24}$	13.84	7.27	4.39	−2.15	−2.25	0.22	−3.89	−5.39	−8.05	−11.51
$C_{25}$	−1.59	−1.43	−0.70	−0.20	5.16	2.07	2.26	2.76	2.53	3.48
$C_{26}$	5.36	1.23	−0.07	−1.64	−4.46	−0.02	0.22	−0.07	−0.17	−0.44
$C_{34}$	9.01	13.07	17.19	21.87	30.25	27.14	31.08	33.21	35.92	37.41
$C_{35}$	13.55	19.56	17.36	18.68	22.56	35.36	40.21	41.38	42.78	44.11
$C_{36}$	−1.04	2.81	4.39	4.43	8.14	−1.13	−1.87	−2.45	−2.99	−3.34
$C_{45}$	6.64	5.73	6.59	9.19	8.81	1.82	−0.54	−2.20	0.78	2.64
$C_{46}$	−8.25	−8.19	−8.26	−8.13	−7.39	−5.95	−5.93	−5.73	−5.97	−6.61
$C_{56}$	3.37	3.70	3.93	5.73	7.45	4.61	3.73	3.14	3.47	3.04

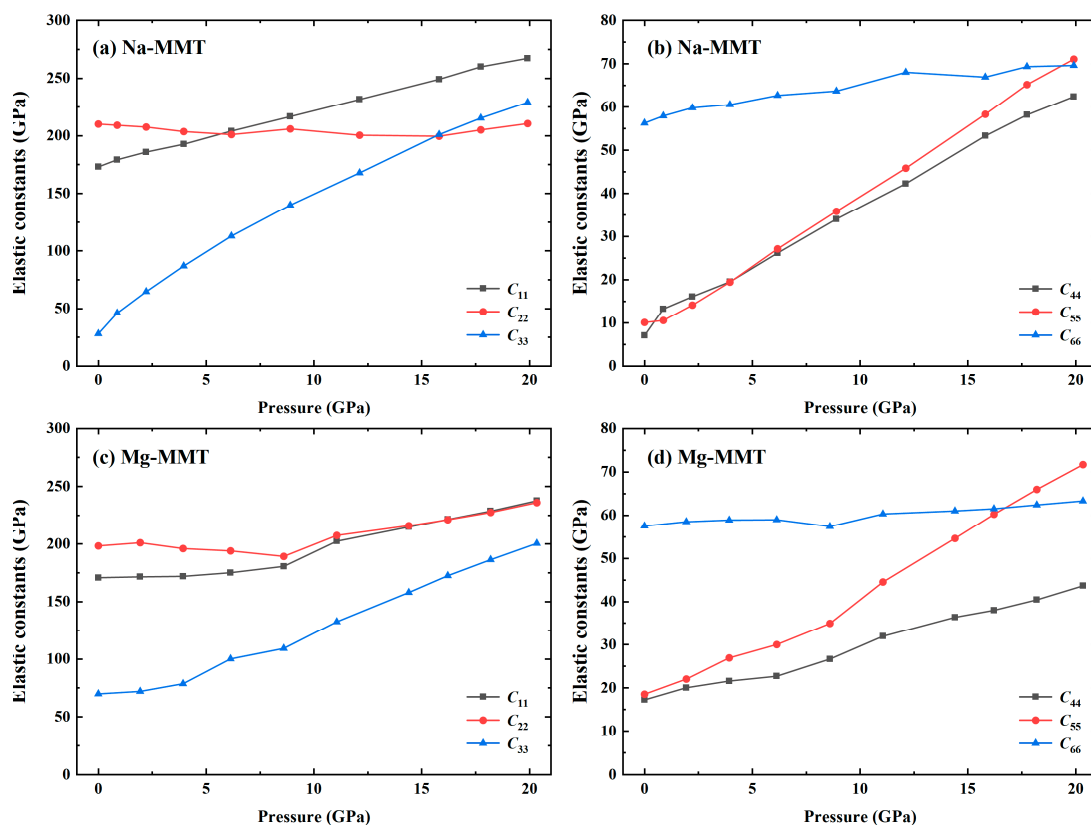


**Figure 8.** The calculated elastic constants ( $C_{ij}$ ) of the Na-MMT and Mg-MMT under different pressures. (a) Calculated value of  $C_{11}$ ,  $C_{22}$  and  $C_{33}$  of Na-MMT under given pressures; (b) calculated value of  $C_{44}$ ,  $C_{55}$  and  $C_{66}$  of Na-MMT under given pressures; (c) calculated value of  $C_{11}$ ,  $C_{22}$  and  $C_{33}$  of Mg-MMT under given pressures; (d) calculated value of  $C_{44}$ ,  $C_{55}$  and  $C_{66}$  of Mg-MMT under given pressures.

The mechanical parameters of montmorillonite under various pressures were obtained by calculating the elastic constants, and values were listed in Tables 13 and 14, were plotted in Figure 9. It can be seen that  $B$ ,  $Y$ ,  $G$ ,  $V_p$ ,  $V_s$  of Na-MMT and Mg-MMT increased gradually with increasing the pressure, and these parameters of Na-MMT increased faster than that of Mg-MMT. The Poisson’s ratio of Mg-MMT increased with increasing the pressure while the Poisson’s ratio of Na-MMT changed little and tended to be flat. Meanwhile, the  $G/B$  of Mg-MMT tended to decrease with the increase of pressure, but the  $G/B$  of Na-MMT had a small change range. The Vicker’s hardness of Mg-MMT increased obviously with the increase of pressure in the range of 0–6.13 GPa. Then, the Vicker’s hardness decreased slowly with increasing the pressure in the range of 6.13 GPa to 20.34 GPa, and the change of curve was very gentle. However, the Vicker’s hardness of Na-MMT increased gradually with the increase of pressure and different from the values of Mg-MMT.

**Table 13.** The calculated bulk modulus ( $B$ ), shear modulus ( $G$ ), Young’s modulus ( $Y$ ), Poisson’s ratio ( $\mu$ ), Pugh’s modulus ( $G/B$ ), Vicker’s hardness ( $H_v$ ), compression wave velocity ( $V_p$ ), and shear wave velocity ( $V_s$ ) of the Na-MMT at given pressure.

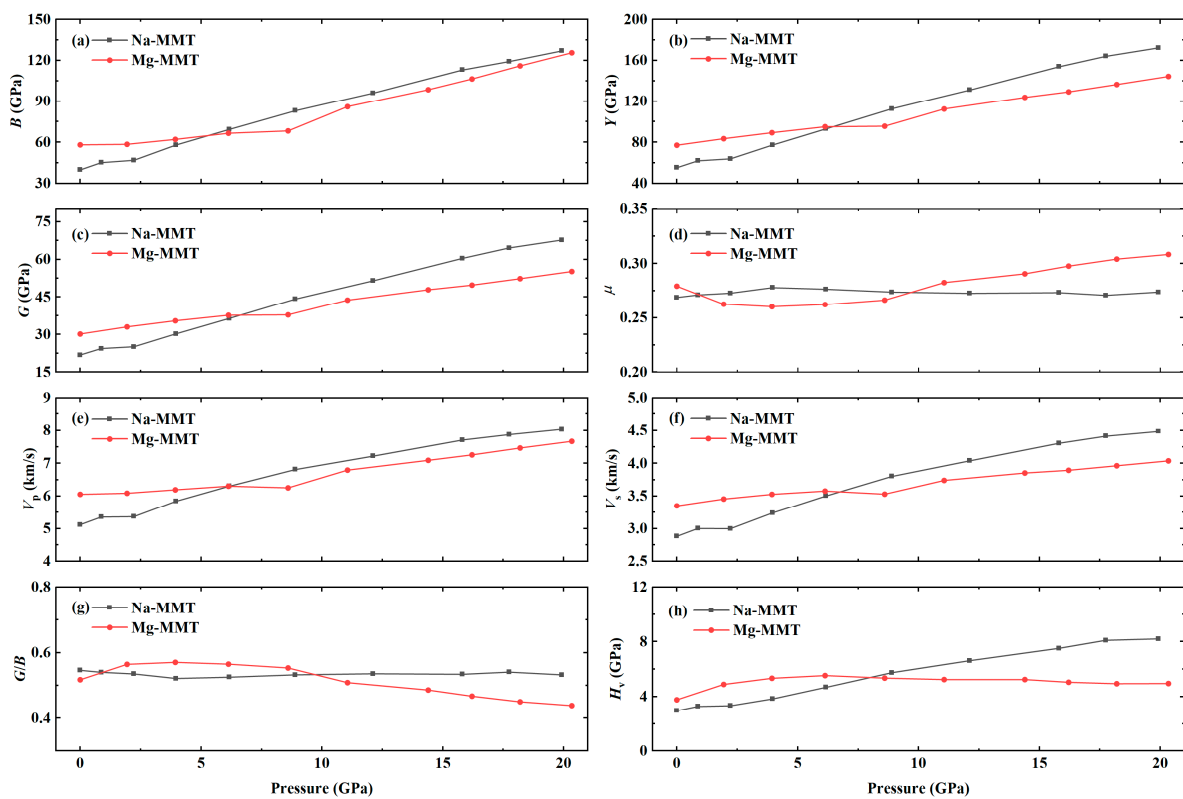
Pressure (GPa)	0	0.87	2.22	3.96	6.17	8.90	12.12	15.81	17.74	19.92
$B$ (GPa)	39.85	45.13	46.88	57.97	69.29	82.93	95.98	113.09	119.29	127.02
$Y$ (GPa)	55.27	61.97	63.91	77.28	92.93	112.56	130.95	153.81	164.03	172.39
$G$ (GPa)	21.78	24.38	25.11	30.24	36.40	44.18	51.45	60.40	64.54	67.67

Table 13. Cont.

Pressure (GPa)	0	0.87	2.22	3.96	6.17	8.90	12.12	15.81	17.74	19.92
$\mu$	0.269	0.271	0.273	0.278	0.277	0.274	0.273	0.273	0.271	0.274
$V_p$ (km/s)	5.12	5.36	5.40	5.85	6.30	6.81	7.22	7.71	7.87	8.03
$V_s$ (km/s)	2.88	3.00	3.00	3.24	3.50	3.80	4.04	4.30	4.41	4.48
$G/B$	0.547	0.540	0.536	0.522	0.525	0.533	0.536	0.534	0.541	0.533
$H_v$ (GPa)	2.96	3.28	3.32	3.83	4.68	5.74	6.62	7.51	8.09	8.20

**Table 14.** The calculated bulk modulus ( $B$ ), shear modulus ( $G$ ), Young's modulus ( $Y$ ), Poisson's ratio ( $\mu$ ), Pugh's modulus ( $G/B$ ), Vicker's hardness ( $H_v$ ), compression wave velocity ( $V_p$ ), and shear wave velocity ( $V_s$ ) of the Mg-MMT at given pressure.

Pressure (GPa)	0	1.94	3.93	6.13	8.60	11.06	14.40	16.21	18.20	20.34
$B$ (GPa)	58.14	58.53	62.11	66.58	68.24	86.04	98.46	106.45	116.09	125.67
$Y$ (GPa)	77.09	83.40	89.37	95.02	95.68	112.29	123.70	129.20	136.49	144.46
$G$ (GPa)	30.13	33.03	35.46	37.64	37.78	43.78	47.92	49.78	52.33	55.21
$\mu$	0.279	0.263	0.260	0.262	0.266	0.282	0.291	0.298	0.304	0.308
$V_p$ (km/s)	6.06	6.09	6.20	6.30	6.26	6.79	7.09	7.26	7.47	7.67
$V_s$ (km/s)	3.35	3.46	3.53	3.58	3.53	3.74	3.85	3.90	3.96	4.04
$G/B$	0.518	0.564	0.571	0.565	0.554	0.509	0.487	0.468	0.451	0.439
$H_v$ (GPa)	3.76	4.89	5.33	5.53	5.34	5.24	5.24	5.05	4.94	4.94



**Figure 9.** The calculated value of elastic modulus, Poisson's ratio, wave velocity, Vicker's hardness and Push's modulus of Na-MMT and Mg-MMT under different pressure. (a) Bulk modulus ( $B$ ); (b) Young's modulus ( $Y$ ); (c) shear modulus ( $G$ ); (d) Poisson's ratio ( $\mu$ ); (e) compression wave velocity ( $V_p$ ); (f) shear wave velocity ( $V_s$ ); (g) Push's modulus ( $G/B$ ); (h) Vicker's hardness ( $H_v$ ).

#### 4. Conclusions

In the present paper, the Vienna Ab-initio Simulation Package based on first-principle and density functional theory with dispersion correction was used to calculate the structural, mechanical and electronic properties of Na-MMT and Mg-MMT under high pressure. The main conclusions are summarized as follows:

1. The calculated structural parameters of Na-MMT and Mg-MMT have been compared favorably with available experimental measurements and other theoretical works at ideal condition. With increasing the pressure, the volume, lattice parameters, and major bond lengths of Na-MMT and Mg-MMT decreased gradually, indicating that the effects of pressure on atomic structure is obvious.
2. The charge density distribution, density of states, and band structure of Na-MMT and Mg-MMT were calculated from 0 GPa to 20 GPa. With increasing the pressure, the charge density distribution and density of states changed slightly, while the width of the band gap was broadened of Na-MMT and Mg-MMT. The results implied that the electronic property of montmorillonite changed slightly under high pressure.
3. The calculated results of mechanical properties at zero pressure are in good agreement with the experimental values, which proves the reliability of the calculation. The major elastic constants of Na-MMT and Mg-MMT were increasing with increasing the pressure. As a result, the mechanical parameters of Bulk modulus, Shear modulus, and Young's modulus increased with increasing the pressure, indicating the elastic mechanics of montmorillonite was significantly improved. Especially, the elastic modulus of Na-MMT increased more rapidly than that of Mg-MMT.

**Author Contributions:** Conceptualization and methodology, J.Z. and Y.C.; software, J.Z.; validation, formal analysis, data curation, and writing, J.Z., Y.C., and L.W.; investigation, J.Z., Y.C., and M.-C.H.; funding acquisition, H.-J.Z. All authors have read and agreed to the published version of the manuscript.

**Funding:** This research was funded by the National Natural Science Foundation of China (No. 41702317), Key Laboratory of ROCK Mechanics and Geohazards of Zhejiang Province (ZJRMG-2019-10), the Fundamental Research Funds for the central universities (2021YQSB02), and National Training Program of Innovation and Entrepreneurship for undergraduates.

**Data Availability Statement:** The data presented in this study are available on request from the first author (zhaojian@cumtb.edu.cn).

**Conflicts of Interest:** The authors declare no conflict of interest.

#### References

1. Aldersley, M.F.; Joshi, P.C.; Price, J.D.; Ferris, J.P. The role of montmorillonite in its catalysis of RNA synthesis. *Appl. Clay Sci.* **2011**, *54*, 1–14. [[CrossRef](#)]
2. Neubauer, V.; Humer, E.; Mann, E.; Kröger, I.; Reisinger, N.; Wagner, M.; Zebeli, Q.; Petri, R.M. Effects of clay mineral supplementation on particle-associated and epimural microbiota, and gene expression in the rumen of cows fed high-concentrate diet. *Anaerobe* **2019**, *59*, 38–48. [[CrossRef](#)]
3. Özdemir, G.; Yapar, S. Preparation and characterization of copper and zinc adsorbed cetylpyridinium and N-lauroylsarcosinate intercalated montmorillonites and their antibacterial activity. *Colloids Surf. B Biointerfaces* **2020**, *188*, 110791. [[CrossRef](#)]
4. Arabkhani, P.; Asfaram, A.; Ateia, M. Easy-to-prepare graphene oxide/sodium montmorillonite polymer nanocomposite with enhanced adsorption performance. *J. Water Process Eng.* **2020**, *38*, 101651. [[CrossRef](#)]
5. Zou, Y.; Zhang, R.; Wang, L.; Xue, K.; Chen, J. Strong adsorption of phosphate from aqueous solution by zirconium-loaded Ca-montmorillonite. *Appl. Clay Sci.* **2020**, *192*, 105638. [[CrossRef](#)]
6. Uddin, F. *Current Topics in the Utilization of Clay in Industrial and Medical Applications*; IntechOpen: London, UK, 2018; Chapter 1.
7. Bergaya, F.; Lagaly, G. *Developments in Clay Science*; Bergaya, F., Lagaly, G., Eds.; Elsevier: Amsterdam, The Netherlands, 2013; Volume 5, pp. 1–19.
8. Zhu, R.; Chen, Q.; Zhou, Q.; Xi, Y.; Zhu, J.; He, H. Adsorbents based on montmorillonite for contaminant removal from water: A review. *Appl. Clay Sci.* **2016**, *123*, 239–258. [[CrossRef](#)]
9. Maryan, A.S.; Montazer, M. Natural and organo-montmorillonite as antibacterial nanoclays for cotton garment. *J. Ind. Eng. Chem.* **2015**, *22*, 164–170. [[CrossRef](#)]

10. Zhou, D.; Zhang, Z.; Tang, J.; Wang, F.; Liao, L. Applied properties of oil-based drilling fluids with montmorillonites modified by cationic and anionic surfactants. *Appl. Clay Sci.* **2016**, *121–122*, 1–8. [[CrossRef](#)]
11. Wang, Y.; Lu, F.; Li, Y.; Wu, T.; Sun, D.; Zhang, G.; Huang, X.; Wang, G. Effects of Na–montmorillonite particles on the emulsification stability of polymer flooding produced water. *Colloids Surf. A Physicochem. Eng. Asp.* **2012**, *410*, 125–129. [[CrossRef](#)]
12. Weng, Z.; Wang, J.; Senthil, T.; Wu, L. Mechanical and thermal properties of ABS/montmorillonite nanocomposites for fused deposition modeling 3D printing. *Mater. Des.* **2016**, *102*, 276–283. [[CrossRef](#)]
13. Asgari, M.; Abouelmagd, A.; Sundararaj, U. Silane functionalization of sodium montmorillonite nanoclay and its effect on rheological and mechanical properties of HDPE/clay nanocomposites. *Appl. Clay Sci.* **2017**, *146*, 439–448. [[CrossRef](#)]
14. Yang, F.; Mubarak, C.; Keiegel, R.; Kannan, R.M. Supercritical carbon dioxide (scCO<sub>2</sub>) dispersion of poly (ethylene terephthalate)/clay nanocomposites: Structural, mechanical, thermal, and barrier properties. *J. Appl. Polym. Sci.* **2017**, *134*, 1–11. [[CrossRef](#)]
15. Ammar, A.; Elzatahry, A.; Al-Maadeed, M.; Alenizi, A.M.; Huq, A.F.; Karim, A. Nanoclay compatibilization of phase separated polysulfone/polyimide films for oxygen barrier. *Appl. Clay Sci.* **2017**, *137*, 123–134. [[CrossRef](#)]
16. Ma, Y.; Lv, L.; Guo, Y.; Fu, Y.; Shao, Q.; Wu, T.; Guo, S.; Sun, K.; Guo, X.; Wujcik, E.K.; et al. Porous lignin based poly (acrylic acid)/organo-montmorillonite nanocomposites: Swelling behaviors and rapid removal of Pb (II) ions. *Polymer* **2017**, *128*, 12–23. [[CrossRef](#)]
17. Hofmann, U.; Endell, K.; Wilm, D. Kristallstruktur und Quellung von Montmorillonit. *Z. Krist. Cryst. Mater.* **1933**, *86*, 340–348. [[CrossRef](#)]
18. Mooney, R.W.; Keenan, A.G.; Wood, L.A. Adsorption of Water Vapor by Montmorillonite. II. Effect of Exchangeable Ions and Lattice Swelling as Measured by X-Ray Diffraction. *J. Am. Chem. Soc.* **1952**, *74*, 1371–1374. [[CrossRef](#)]
19. Cowley, J.M.; Goswami, A. Electron Diffraction Patterns from Montmorillonite. *Acta Crystallogr.* **1961**, *14*, 1071–1079. [[CrossRef](#)]
20. Nadeau, P.H.; Wilson, M.J.; Mchardy, W.J.; Tait, J.M. Interstratified Clays as Fundamental Particles. *Science* **1984**, *225*, 923–925. [[CrossRef](#)] [[PubMed](#)]
21. Wang, Z.; Wang, H.; Cates, M.E. Effective elastic properties of solid clays. *Geophysics* **2001**, *66*, 428–440. [[CrossRef](#)]
22. Vanorio, T.; Prasad, M.; Nur, A. Elastic properties of dry clay mineral aggregates, suspensions and sandstones. *Geophys. J. Int.* **2003**, *155*, 319–326. [[CrossRef](#)]
23. Mondol, N.H.; Jahren, J.; Bjørlykke, K.; Brevik, I. Elastic properties of clay minerals. *Lead. Edge* **2008**, *27*, 758–770. [[CrossRef](#)]
24. Bridgeman, C.H. Ab-initio total energy study of uncharged 2:1 clays and their interaction with water. *Mol. Phys.* **1996**, *89*, 879–888. [[CrossRef](#)]
25. Refson, K.; Park, S.H.; Sposito, G. Ab Initio Computational Crystallography of 2:1 Clay Minerals: 1. Pyrophyllite-1Tc. *J. Phys. Chem. B* **2003**, *107*, 3376–13383. [[CrossRef](#)]
26. Zartman, G.D.; Liu, H.; Akdim, B.; Pachter, R.; Heinz, H. Nanoscale Tensile, Shear, and Failure Properties of Layered Silicates as a Function of Cation Density and Stress. *J. Phys. Chem. C* **2010**, *114*, 1763–1772. [[CrossRef](#)]
27. Chatterjee, A.; Iwasaki, T.; Hayashi, H.; Ebina, T.; Torii, K. Electronic and structural properties of montmorillonite—A quantum chemical study. *J. Mol. Catal. A Chem.* **1998**, *136*, 195–202. [[CrossRef](#)]
28. Sainz-Díaz, C.I.; Timón, V.; Botella, V.; Artacho, E.; Hernández-Laguna, A. Quantum mechanical calculations of dioctahedral 2:1 phyllosilicates: Effect of octahedral cation distributions in pyrophyllite, illite, and smectite. *Am. Mineral.* **2002**, *87*, 958–965. [[CrossRef](#)]
29. Chatterjee, A.; Ebina, T.; Onodera, Y.; Mizukami, F. Effect of exchangeable cation on the swelling property of 2:1 dioctahedral smectite—A periodic first principle study. *J. Chem. Phys.* **2004**, *120*, 3414–3424. [[CrossRef](#)] [[PubMed](#)]
30. Berghout, A.; Tunega, D.; Zaoui, A. Density Functional Theory (DFT) Study of the Hydration Steps of Na<sup>+</sup>/Mg<sup>2+</sup>/Ca<sup>2+</sup>/Sr<sup>2+</sup>/Ba<sup>2+</sup>-Exchanged Montmorillonites. *Clays Clay Miner.* **2010**, *58*, 174–187. [[CrossRef](#)]
31. Kresse, G.; Hafner, J. Ab initio molecular dynamics for open-shell transition metals. *Phys. Rev. B Condens. Matter* **1993**, *48*, 13115–13118. [[CrossRef](#)]
32. Kresse, G.; Furthmüller, J. Efficiency of ab-initio total energy calculations for metals and semiconductors using a plane-wave basis set. *Comput. Mater. Sci.* **1996**, *6*, 15–50. [[CrossRef](#)]
33. Blöchl, P.E. Projector augmented-wave method. *Phys. Rev. B Condens. Matter* **1994**, *50*, 17953–17979. [[CrossRef](#)] [[PubMed](#)]
34. Perdew, J.P.; Burke, K.; Ernzerhof, M. Generalized Gradient Approximation Made Simple. *Phys. Rev. Lett.* **1996**, *77*, 3865–3868. [[CrossRef](#)]
35. Grimme, S. Semiempirical GGA-Type Density Functional Constructed with a Long-Range Dispersion Correction. *J. Comput. Chem.* **2006**, *27*, 1787–1799. [[CrossRef](#)]
36. Monkhorst, H.J.; Pack, J.D. Special points for Brillouin-zone integrations. *Phys. Rev. B* **1976**, *13*, 5188–5192. [[CrossRef](#)]
37. Benazzouz, B.K.; Zaoui, A. Phase diagram of kaolinite from Molecular Dynamics calculations. *Phys. B Condens. Matter* **2012**, *407*, 2462–2470. [[CrossRef](#)]
38. Hill, R. The Elastic Behaviour of a Crystalline Aggregate. *Proc. Phys. Soc. A* **1952**, *65*, 349–354. [[CrossRef](#)]
39. Zhou, C.; Tong, D.; Yu, W. *Nanomaterials from Clay Minerals*; Wang, A., Wang, W., Eds.; Elsevier: Amsterdam, The Netherlands, 2019; pp. 335–364.
40. Tsiপুরsky, S.I.; Drits, V. The Distribution of Octahedral Cations in the 2:1 Layers of Dioctahedral Smectites Studied by Oblique-Texture Electron Diffraction. *Clay Miner.* **1984**, *19*, 177–193. [[CrossRef](#)]

- 
41. Voora, V.K.; Al-Saidi, W.A.; Jordan, K.D. Density Functional Theory Study of Pyrophyllite and M-Montmorillonites (M = Li, Na, K, Mg, and Ca): Role of Dispersion Interactions. *J. Phys. Chem. A* **2011**, *115*, 9695–9703. [[CrossRef](#)] [[PubMed](#)]
  42. Pugh, S. XCII. Relations between the elastic moduli and the plastic properties of polycrystalline pure metals. *Philos. Mag. Ser.* **1954**, *45*, 823–843. [[CrossRef](#)]
  43. Wang, Z. Fundamentals of seismic rock physics. *Geophysics* **2001**, *66*, 398–412. [[CrossRef](#)]